Materials Transactions, Vol. 50, No. 5 (2009) pp. 1023 to 1031
Special Issue on Nano-Materials Science for Atomic Scale Modification
©2009 The Japan Institute of Metals

Mass-Transfer Mechanism of Alumina Ceramics under Oxygen Potential Gradients at High Temperatures

Satoshi Kitaoka, Tsuneaki Matsudaira and Masashi Wada

Japan Fine Ceramics Center, Nagoya 456-8587, Japan

The oxygen permeability of an undoped polycrystalline α-Al_2O_3 wafer that was exposed to oxygen potential gradients was evaluated at temperatures up to 1973 K. Oxygen preferentially permeated through the grain boundaries of α-Al_2O_3. The main diffusion species, which were attributed to oxygen permeation, depended on oxygen partial pressures (P_{O_2}), forming oxygen potential gradients. Under oxygen potential gradients generated by P_{O_2} below about 1 Pa, oxygen permeation occurred by oxygen diffusing from regions of higher P_{O_2} to regions of lower P_{O_2}. By contrast, under oxygen potential gradients generated by P_{O_2} above about 1 Pa, oxygen permeation proceeded by aluminum diffusing from regions of lower P_{O_2} to regions of higher P_{O_2}. In other words, O_2 molecules were adsorbed onto a surface at higher P_{O_2} and subsequently dissociated into oxygen ions (forming Al_2O_3), while oxygen ions on the opposite surface at lower P_{O_2} were desorbed by association into O_2 molecules (decomposition of Al_2O_3). The grain-boundary diffusion coefficients of oxygen and aluminum as a function of P_{O_2} were determined from the oxygen permeation constants. [doi:10.2320/matertrans.MC200803]

(Received November 4, 2008; Accepted February 18, 2009; Published April 25, 2009)

Keywords: *Al_2O_3, oxygen permeation, oxygen potential gradient, diffusion, grain boundary*

1. Introduction

Thermal barrier coatings (TBCs) are widely used for hot section components of gas turbine engines to protect the underlying metals from the high operating temperatures; they serve to both increase the engine efficiency and improve the durability of components. TBC systems typically consist of a Ni-based superalloy substrate, an alumina forming-alloy bond coat and an yttria-stabilized zirconia topcoat. When TBCs are exposed to high temperatures in oxidizing environments, a thermally grown oxide (TGO) develops on the bond coat surface underneath the top coat. Fracture of TBCs progresses in the vicinity of the TGO, which attains a critical thickness during thermal cycling operations.[1] The TGO generally consists of a dense α-Al_2O_3 scale, which functions as a protective layer,[2] and a non-protective oxide layer, such as (Co, Ni)(Al, Cr)$_2O_4$ or (Co, Ni)O, which is believed to promote the spalling of TBCs.[3–7] Thus, suppressing mass-transfer through the α-Al_2O_3 scale is anticipated to further improve the durability of TBCs.

When a solid oxide is placed in an oxygen potential gradient generated by a combination of different oxygen partial pressures (P_{O_2}), a cation potential gradient is generally induced in the opposite direction to the oxygen potential gradient in accordance with the Gibbs-Duhem equation. Thus, the cation migrates from areas of low P_{O_2} to areas of high P_{O_2}, in the opposite direction to the migration of oxygen ions, resulting in the oxide as a whole shifting toward higher P_{O_2}.[8,9] If the cation migration occurs mainly along the grain boundaries of the oxide, grain boundary ridges will develop on the higher P_{O_2} side. The α-Al_2O_3 scale, which is exposed to steep oxygen potential gradients, is grown on the alumina forming alloys by the inward diffusion of oxygen and the outward diffusion of aluminum, resulting in progressive oxidation of the alloys. When oxidation of the alloys occurs through the α-Al_2O_3 scale in air, grain boundary ridges develop on the scale surface by outward grain boundary diffusion of aluminum. By contrast, when oxidation of the alloys occurs through the α-Al_2O_3 scale in gases such as purified argon, the ridges are not present.[10] Ridge formation (i.e., mass-transfer through the Al_2O_3 scale) is thought to be dependent on the P_{O_2}.

Many studies have investigated oxygen grain boundary diffusion in polycrystalline α-Al_2O_3 by using either secondary ion mass spectroscopy (SIMS)[11–13] or nuclear reaction analysis (NRA)[14] to determine ^{18}O depth profiles after high temperature exchange with ^{18}O-enriched oxygen. Messaoudi *et al.* had reported that the oxygen grain boundary diffusion coefficients are determined from the transport through the growing Al_2O_3 scale.[13] This is done by oxidizing the alumina forming alloys in an $^{16}O_2$ atmosphere, further oxidizing them in $^{18}O_2$ and then determining the ^{18}O distribution in the α-Al_2O_3 scale using SIMS. The oxygen grain boundary diffusion coefficients determined by this procedure are larger than those determined from extrapolated diffusion data for polycrystalline α-Al_2O_3 annealed in a homogeneous environment without any oxygen potential gradients.[11,12,14] The corresponding activation energies[13] derived by the double oxidation technique are smaller than those for obtained by annealing.[11,12,14] It is currently unclear why these phenomena are induced by oxygen potential gradients.

On the other hand, there have been no reports of measurements of aluminum grain boundary diffusion coefficients in Al_2O_3, either with or without oxygen potential gradients, and there have been only two reports of measurements of aluminum lattice diffusion coefficients.[15,16] In this case, the appropriate tracer ^{26}Al has a very low specific activity and an extremely long half-life of 7.2×10^5 years, making it very difficult to perform radiotracer diffusion experiments. Nychka *et al.*,[10] then, deduced the aluminum grain boundary flux through an Al_2O_3 scale during oxidation of alumina forming alloys by measuring the scale thickness, which consisted of double layers, such as equiaxial grains produced by outward diffusion of aluminum and underlying columnar grains developed by inward diffusion of oxygen.

The diffusion coefficients of species in solid oxides are generally proportional to their defect concentrations, which depend on the P_{O_2} of the atmosphere to which the oxides are exposed. The lattice diffusion coefficients of iron and oxygen in magnetite actually exhibited a strong dependence on the P_{O_2}.[17,18] Ueda *et al.*[8] reported that the effective diffusion coefficients of iron and oxygen, which include both lattice diffusion and grain boundary diffusion in a magnetite scale formed on iron, were influenced by the oxygen potential gradient in the scale. For Al_2O_3 scale on alumina forming alloys, therefore, the diffusion coefficients of both aluminum and oxygen are also presumed to be affected by the oxygen potential gradient in the scale. However, there have been no studies on the P_{O_2} dependence of the diffusion coefficients of either aluminum or oxygen.

Alumina forming alloys contain small quantities of oxygen-reactive elements (REs) (e.g., Y, La, Ti, Zr, and Hf) to improve the oxidation resistance of the alloys. These REs segregate at grain boundaries in growing Al_2O_3 scales during oxidation of the alloys and diffuse toward the scale/gas interface, resulting in the precipitation of RE-rich particles.[19] The REs are thought to affect the scale growth by altering both the outward grain boundary diffusion of aluminum and the inward grain boundary diffusion of oxygen.[10] Unfortunately, it is unclear which migration of aluminum and oxygen in the scale the RE ions inhibit, because the difference between the grain boundary diffusivities of aluminum and oxygen has not been determined even in pure α-Al_2O_3. The coexistence of various kinds of REs further complicates the interpretation of experimental results.

The inherent effectiveness of monolithic α-Al_2O_3 as a barrier to oxygen permeation has been estimated directly by measuring the oxygen permeation through a polycrystalline Al_2O_3 wafer exposed to oxygen potential gradients at high temperatures.[20–23] When oxygen potential gradients are produced by a combination of high P_{O_2}, the oxygen permeation is considered to proceed mainly by grain boundary diffusion of aluminum toward the higher P_{O_2} side, resulting in the formation of grain boundary ridges.[20] By contrast, no ridges are observed when oxygen potential gradients are formed by a combination of low P_{O_2}, even when there is sufficient oxygen permeation. The ridge evolution has a similar P_{O_2} dependence as that on a growing Al_2O_3 scale during oxidation of alumina forming alloys.[10] This thus suggests that mass-transfer through the Al_2O_3 wafer is controlled by the P_{O_2} in the oxygen permeation technique.

In this study, the effect of oxygen potential gradients on mass-transfer mechanisms in a non-doped polycrystalline α-Al_2O_3 was elucidated by measuring the oxygen permeability constants through an Al_2O_3 wafer at high temperatures. The grain boundary diffusion coefficients of aluminum and oxygen were calculated from the oxygen permeation data. The oxygen grain boundary diffusion coefficients were also compared with literature data determined using the isotropic tracer profiling.

2. Experimental Procedures

2.1 Materials

Commercial, high-purity α-Al_2O_3 powder (TM-DAR, Taimei Chemicals Co., Ltd., Nagano, Japan, purity >99.99 mass%) was used to prepare the polycrystals. The α-Al_2O_3 powder was molded by a uniaxial press at 20 MPa and then subjected to cold isostatic pressing at 600 MPa. The green compacts were pressureless sintered in air at 1773 K for 5 h. Wafers with dimensions of $\Phi 23.5 \times 0.25$ mm were cut from the sintered bodies and then polished so that their surfaces had a mirror-like finish. The relative density of the wafers was 99.5% of the theoretical density.

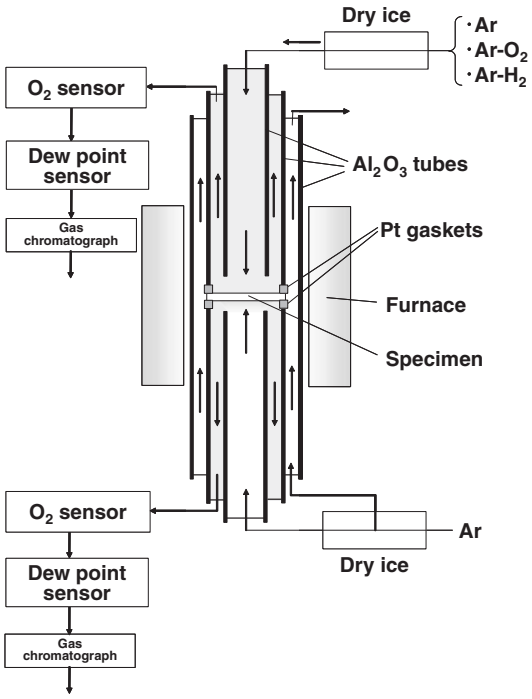

Fig. 1 Schematic diagram of the gas permeability apparatus.

2.2 Oxygen permeability constants

Figure 1 shows a schematic diagram of the oxygen permeability apparatus. A polycrystalline α-Al_2O_3 wafer was set between two alumina tubes in a furnace. Platinum gaskets were used to create a seal between the wafer and the Al_2O_3 tubes by loading a dead weight from the top of the upper tube. A gas-tight seal was achieved by heating at 1893–1973 K under an Ar gas flow for 3 h or more. After that, a P_{O_2} of oxygen included as an impurity in the Ar gas was monitored at the outlets of the upper and lower chambers that enclosed the wafer and the Al_2O_3 tubes using a zirconia oxygen sensor at 973 K. The partial pressure of water vapor (P_{H_2O}) was measured at room temperature using an optical dew point sensor. These measured P_{O_2} and P_{H_2O} were regarded as backgrounds. Then, pure O_2 gas or Ar gas containing either 1–10 vol% O_2 or 0.01–1 vol% H_2 was introduced into the upper chamber at a flow rate of 1.67×10^{-6} m^3/s. A constant flux for oxygen permeation was judged to be achieved when the values of the P_{O_2} and P_{H_2O} monitored in the outlets became constant.

When either O_2 gas or the Ar/O_2 mixture was introduced into the upper chamber and Ar was introduced into the lower chamber to create an oxygen gradient across the wafer, oxygen permeated from the upper chamber to the lower

chamber. The P_{O_2} values in the lower chamber at the experimental temperatures were calculated thermodynamically from the values measured at 973 K. The calculated values were almost the same as those at 973 K. On the other hand, when the Ar/H_2 mixture was introduced into the upper chamber and Ar was introduced into the lower chamber, a tiny amount of oxygen in the Ar permeated from the lower chamber to the upper chamber and reacted with H_2 to form water vapor. As a result, the P_{H_2O} in the upper chamber increased while the H_2 partial pressure (P_{H_2}), which was measured at room temperature by gas chromatography, in the upper chamber decreased. The increase of P_{H_2O} in the upper chamber was comparable to the reduction of P_{O_2} in the lower chamber in terms of oxygen, and the P_{H_2O} in the lower chamber remained constant during the permeation tests; thus, hydrogen permeation from the upper chamber to the lower chamber was negligibly small in comparison with the oxygen permeation in the opposite direction. The P_{O_2} values in the upper chamber at the experimental temperatures were estimated thermodynamically from the P_{H_2O} and P_{H_2} measured at room temperature.

The oxygen permeability constant, PL, was calculated from the difference between the P_{O_2} estimated thermodynamically in one chamber (which had a lower P_{O_2} than that in another chamber) and the background in the lower P_{O_2} chamber using[20,22,23]

$$PL = \frac{C_p \cdot Q \cdot L}{V_{st} \cdot S}, \tag{1}$$

where C_p is the concentration of permeated oxygen (P_{O_2}/P_T, where P_T = total pressure), Q is the flow rate of the test gases, V_{st} is the standard molar volume of an ideal gas, S is the permeation area of the wafer, and L is the wafer thickness.

The wafer surfaces exposed to oxygen potential gradients at 1923 K for 10 h were observed by scanning electron microscopy (SEM). The volume of the grain boundary ridges formed on the surfaces by the oxygen potential gradients was measured by 3D laser scanning microscopy, and was compared with the total amount of the oxygen permeated in the wafer.

2.3 Determination of grain boundary diffusion coefficients

2.3.1 Fluxes of charged particles

Figure 2 shows a schematic representation of the fluxes of charged particles, i, such as Al^{3+}, O^{2-}, electron e' and hole $h^{\cdot}$ in Al_2O_3 under an oxygen potential gradient in which $P_{O_2}(II) > P_{O_2}(I)$.

The charged particle flux is described as

$$J_i = -Z_i\left(\frac{C_i D_i}{RT}\right)\frac{\partial \eta_i}{\partial x}, \tag{2}$$
$$\eta_i = \mu_i + Z_i F\phi,$$

where Z_i is the charge of the diffusing particle, C_i is the molar concentration per unit volume, D_i is the diffusion coefficient, R is the gas constant, T is the absolute temperature, x is the space coordinate, η_i is the electrochemical potential, μ_i is the chemical potential, ϕ is the electrostatic potential and F is the Faraday constant. The Nernst-Einstein relation is given by

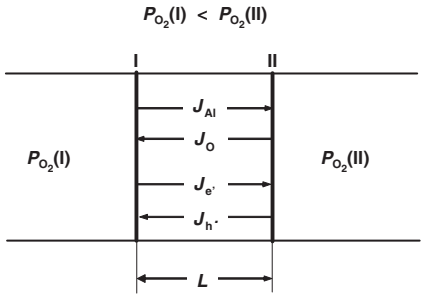

Fig. 2 Schematic representation of charged particle fluxes in Al_2O_3 under an oxygen potential gradient with $P_{O_2}(II) > P_{O_2}(I)$.

$$\sigma t_i = Z_i^2 F^2 \frac{C_i D_i}{RT}, \tag{3}$$

where σ denotes the electrical conductivity and t_i is the transport number, which is defined by

$$t_{Al} + t_O + t_{h^{\cdot}} + t_{e'} = 1. \tag{4}$$

The Gibbs-Duhem equation is expressed by

$$|Z_O| d\mu_{Al} + |Z_{Al}| d\mu_O = 0. \tag{5}$$

The following relation for electrical neutrality should hold for the charged particle fluxes.

$$J_{Al} + J_O + J_{h^{\cdot}} + J_{e'} = 0. \tag{6}$$

The flux of the oxygen that permeates through the wafer is equal to the sum of J_{Al} and J_O. From eqs. (2)–(6), it is concluded that

$$J_{TO} = J_{Al} + J_O = -\left(\frac{Z_{Al}^2}{Z_O} C_{Al} D_{Al} + Z_O C_O D_O\right)\frac{(t_{h^{\cdot}} + t_{e'})}{RT} \cdot \frac{\partial \mu_O}{\partial x}. \tag{7}$$

The oxygen chemical potential μ_O is given by

$$\mu_O = \frac{1}{2}\left(\mu_{O_2}^0 + RT\ ln\ P_{O_2}\right). \tag{8}$$

Substituting eq. (8) into eq. (7) gives

$$J_{TO} = -\left(\frac{Z_{Al}^2}{Z_O} C_{Al} D_{Al} + Z_O C_O D_O\right)\frac{(t_{h^{\cdot}} + t_{e'})}{2} \times \frac{d\ ln\ P_{O_2}}{dx}. \tag{9}$$

Integrating eq. (9) from $x = 0$ to $x = L$ gives

$$\int_0^L J_{TO} dx = -\frac{(t_{h^{\cdot}} + t_{e'})}{2}\left(\frac{Z_{Al}^2 C_{Al}}{Z_O}\int_{P_{O_2}(I)}^{P_{O_2}(II)} D_{Al} d\ ln\ P_{O_2} + Z_O C_O \int_{P_{O_2}(I)}^{P_{O_2}(II)} D_O d\ ln\ P_{O_2}\right) \tag{10}$$

Equation (10) is applicable for the case of ideal oxygen permeation when there is no interaction between the electrons and holes, or when either electrons or holes participate.

2.3.2 *n*-type conduction

The flux of the oxygen that permeates through the wafer is postulated to be equal only to J_O. It is also assumed that oxygen permeates only through reactions between defects, in which both oxygen vacancies and electrons participate. In

these reactions, dissociative adsorption of O_2 molecules is assumed to progress on the surface exposed to the higher P_{O_2} (i.e., P_{O_2}(II)) as follows.

$$1/2O_2 + V_O^{\bullet\bullet} + 2e' \rightarrow O_O^x \quad (11)$$

Oxygen ions migrate through oxygen vacancies from the P_{O_2}(II) side to the lower P_{O_2} side (i.e., P_{O_2}(I)), and oxygen vacancies and electrons diffuse in the opposite direction to the oxygen flux. The inverse reaction to eq. (11) proceeds on the P_{O_2}(I) surface, and oxygen ions recombine to produce O_2 molecules.

The equilibrium constant of the reaction (eq. (11)) can be expressed as follows

$$K_{V_O^{\bullet\bullet}} = \frac{1}{4[V_O^{\bullet\bullet}]^3} P_{O_2}{}^{-1/2} \quad (12)$$

According to $C_O D_O = [V_O^{\bullet\bullet}] D_{V_O^{\bullet\bullet}}$, where $D_{V_O^{\bullet\bullet}}$ is the diffusion coefficient of oxygen vacancies, eq. (12) can be written as

$$D_O = \frac{D_{V_O^{\bullet\bullet}}}{C_O} \left(\frac{1}{4K_{V_O^{\bullet\bullet}}}\right)^{1/3} P_{O_2}{}^{-1/6} \quad (13)$$

If the diffusing species migrate mainly along the grain boundaries of polycrystalline Al_2O_3, eq. (13) can be rewritten as

$$D_{Ogb}\delta = \frac{D_{V_{Ogb}^{\bullet\bullet}}}{C_{Ob} S_{gb}} \left(\frac{1}{4K_{V_{Ogb}^{\bullet\bullet}}}\right)^{1/3} P_{O_2}{}^{-1/6} \quad (14)$$

where D_{Ogb} is the grain boundary diffusion coefficient of oxygen, δ is the grain boundary width, C_{Ob} is the molar concentration of oxygen per unit volume, S_{gb} is the grain boundary density, which is determined from the average grain size of the Al_2O_3. $D_{V_{Ogb}^{\bullet\bullet}}$ is the grain boundary diffusion coefficient of an oxygen vacancy, $K_{V_{Ogb}^{\bullet\bullet}}$ is the equilibrium constant of reaction (11) that occurs at grain boundaries. Assuming that $t_{e'} = 1$ and $D_{Ogb} \gg D_{Algb}$, and inserting $Z_O = -2$ and eq. (14) into eq. (10) gives

$$\int_0^L J_{TO} dx = A_O (P_{O_2}(II)^{-1/6} - P_{O_2}(I)^{-1/6}) \quad (15)$$

$$A_O = -6\left(\frac{1}{4K_{V_{Ogb}^{\bullet\bullet}}}\right)^{1/3} D_{V_{Ogb}^{\bullet\bullet}}$$

Equation (15) can be expressed in terms of the oxygen permeability constant, PL, defined by eq. (1) as follows.

$$\int_0^L J_{TO} dx = 4PL \quad (16)$$

If the constant A_O is determined experimentally using eqs. (15) and (16), $D_{Ogb}\delta$ for a certain P_{O_2} can be estimated from eq. (14).

2.3.3 *p*-type conduction

The flux of the oxygen that permeates through the wafer is premised to be equal only to J_{Al}. Oxygen permeation is also assumed to occur by reactions in which both aluminum vacancies and holes participate. O_2 molecules are absorbed on the surface exposed to P_{O_2}(II) as follows.

$$1/2O_2 \rightarrow O_O^X + 2/3V_{Al}^{'''} + 2h^{\cdot} \quad (17)$$

Aluminum vacancies move from the P_{O_2}(II) side to the P_{O_2}(I) side, and aluminum ions and holes migrate in the opposite direction. Finally, the inverse reaction of (17) occurs on the P_{O_2}(I) surface, and oxygen ions recombine to produce an O_2 molecule.

In a similar way to Section 2.3.2, the grain boundary diffusion coefficient of aluminum, D_{Algb}, is obtained as follows.

$$D_{Algb}\delta = \frac{D_{V_{Algb}^{'''}}}{C_{Alb} S_{gb}} \left(\frac{K_{V_{Algb}^{'''}}}{9}\right)^{3/8} P_{O_2}{}^{3/16} \quad (18)$$

C_{Alb} denotes the molar concentration of aluminum per unit volume, $D_{V_{Algb}^{'''}}$ is the grain boundary diffusion coefficient of aluminum vacancies, $K_{V_{Algb}^{'''}}$ is the equilibrium constant of reaction (17) that occurs at the grain boundaries. If it is assumed that $t_{h^{\cdot}} = 1$ and $D_{Algb} \gg D_{Ogb}$, then substituting $Z_{Al} = +3$ and $Z_O = -2$ into eq. (10) gives

$$\int_0^L J_{TO} dx = A_{Al}(P_{O_2}(II)^{3/16} - P_{O_2}(I)^{3/16}) = 4PL \quad (19)$$

$$A_{Al} = 12\left(\frac{K_{V_{Algb}^{'''}}}{9}\right)^{3/8} D_{V_{Algb}^{'''}}$$

If the experimental value of A_{Al} is obtained using eq. (19), $D_{Algb}\delta$ for a certain P_{O_2} can be calculated from eq. (18).

3. Results and Discussion

3.1 Oxygen permeation

Figure 3 shows the temperature dependence of the oxygen permeability constant of polycrystalline Al_2O_3 exposed to an oxygen partial pressure difference (ΔP_{O_2}), where the P_{O_2} in Ar introduced into the lower chamber was roughly constant of 1 Pa, and the P_{O_2} into the upper chamber was greatly varied. The open symbols indicate data for specimens

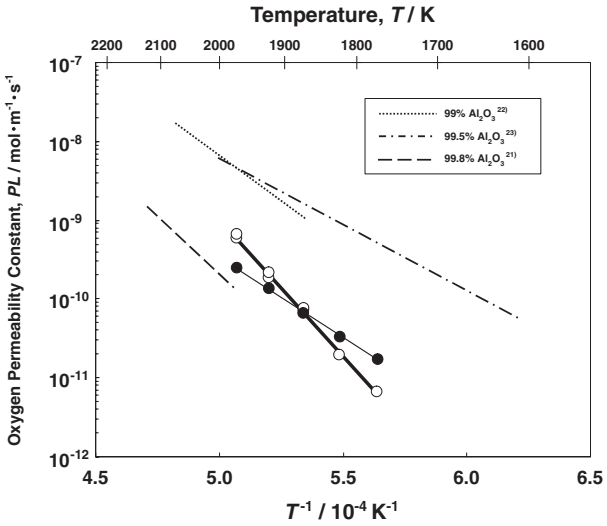

Fig. 3 Temperature dependence of oxygen permeability constant of polycrystalline Al_2O_3 exposed to ΔP_{O_2}. The open symbols indicate data for specimens exposed to a ΔP_{O_2} caused by P_{O_2} between $P_{O_2}(II) = 10^5$ and $P_{O_2}(I) = 1$ Pa. The solid symbols indicate data for a ΔP_{O_2} caused by P_{O_2} between $P_{O_2}(II) = 1$ and $P_{O_2}(I) = 10^{-8}$ Pa. The other lines are data from the literature[21–23] under a similar ΔP_{O_2} as that for the open symbols.

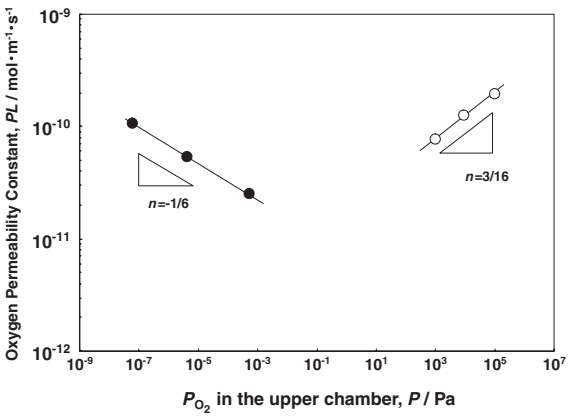

Fig. 4 Effect of P_{O_2} in the upper chamber on the oxygen permeability constants of polycrystalline Al_2O_3 at 1923 K. The solid symbols indicate the data for specimens exposed to a ΔP_{O_2} caused by a $P_{O_2}(II) = 1$ Pa in the lower chamber and a much lower P_{O_2} ($P_{O_2}(I)$) in the upper chamber. The open symbols indicate data for a ΔP_{O_2} caused by a $P_{O_2}(I) = 1$ Pa in the lower chamber and a much higher P_{O_2} ($P_{O_2}(II)$) in the upper chamber.

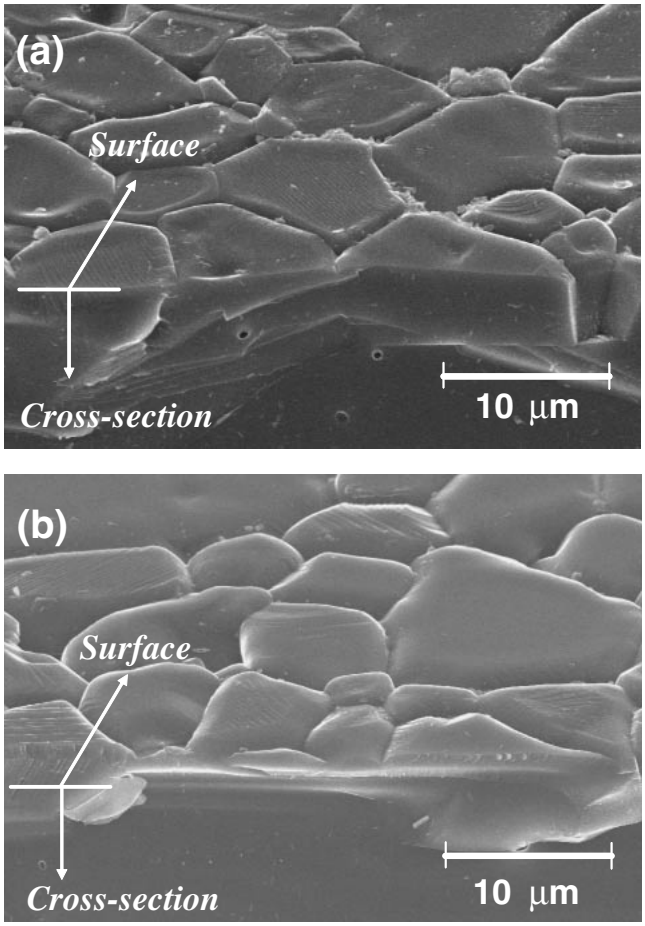

Fig. 5 SEM micrographs of the two surfaces of polycrystalline Al_2O_3 exposed at 1923 K for 10 h under a ΔP_{O_2} with (a) $P_{O_2}(I) = 10^{-8}$ Pa in the upper chamber and (b) $P_{O_2}(II) = 1$ Pa in the lower chamber.

exposed to a ΔP_{O_2} caused by P_{O_2} between $P_{O_2}(II) = 10^5$ and $P_{O_2}(I) = 1$ Pa. The solid symbols indicate data for a ΔP_{O_2} caused by P_{O_2} between $P_{O_2}(II) = 1$ and $P_{O_2}(I) = 10^{-8}$ Pa. The other lines are data from the literature for a ΔP_{O_2} similar to that for the open symbols.[21–23] The oxygen permeability constants increase with increasing temperature, such that they are linear when plotted against T^{-1}, in a similar manner as the data from the literature. The oxygen permeability constants tend to decrease with increasing purity of Al_2O_3. The slopes of these linear rate plots depend on the magnitude of the oxygen potential gradients. This suggests that the oxygen permeation mechanism varies depending on the oxygen potential gradients.

Because the oxygen permeability constants of a single-crystal Al_2O_3 wafer were lower than the measurable limit of this system (below 1×10^{-12} mol·m^{-1} s^{-1} at 1773 K), the oxygen permeation is thought to occur preferentially through the grain boundaries for the polycrystalline Al_2O_3.[20] Furthermore, the oxygen permeability constants of the polycrystalline wafers were inversely proportional to the wafer thickness. According to eq. (2), therefore, the oxygen permeation is considered to be controlled by diffusion in the wafer, not by interfacial reaction between the wafer surfaces and ambient gases.

Figure 4 shows the effect of P_{O_2} in the upper chamber on the oxygen permeability constants of polycrystalline Al_2O_3 at 1923 K. The solid symbols indicate the data for specimens exposed to a ΔP_{O_2} caused by a $P_{O_2}(II) = 1$ Pa in the lower chamber and a much lower P_{O_2} ($P_{O_2}(I)$) in the upper chamber. The open symbols indicate data for a ΔP_{O_2} caused by a $P_{O_2}(I) = 1$ Pa in the lower chamber and a much higher P_{O_2} ($P_{O_2}(II)$) in the upper chamber. The oxygen permeability constants for P_{O_2} below 10^{-3} Pa in the upper chamber decrease with increasing P_{O_2}. This slope corresponds to a power constant of $n = -1/6$. On the other hand, the oxygen permeability constants for P_{O_2} above 10^3 Pa in the upper chamber increase with increasing P_{O_2}, and the slope corresponds to a power constant of $n = 3/16$. It is well known that single-crystal Al_2O_3 exhibits n-type conduction under a low P_{O_2} and p-type conduction under a high P_{O_2} at high temperatures, where the P_{O_2} dependences on the power coefficients have been summarized for various lattice defects.[24,25] The power coefficients of $n = -1/6$ and $3/16$ determined in this study are applicable to the defect reactions given in eqs. (11) and (17), respectively. Therefore, depending on the levels of the P_{O_2} values for the oxygen potential gradients, either eq. (11) or eq. (17) probably applies to a surface exposed to the higher P_{O_2} ($P_{O_2}(II)$), and their inverse reaction seems to proceed on the surface exposed to the lower P_{O_2} ($P_{O_2}(I)$). O_2 molecules are assumed to permeate through the wafer through these serial reactions. As shown in Fig. 4, plots of *log* (oxygen permeability constant) against $log(P_{O_2})$ give straight lines. For this reason, when $P_{O_2}(II) \gg P_{O_2}(I)$, the oxygen permeability constant for a P_{O_2} range of $n = -1/6$ is related to $P_{O_2}(I)$ in accordance with eq. (15), whereas, the permeability constant for a P_{O_2} range of $n = 3/16$ is dominated by $P_{O_2}(II)$ in accordance with eq. (19).

Figure 5 shows SEM micrographs of the two surfaces of an Al_2O_3 wafer exposed at 1923 K for 10 h under a ΔP_{O_2} produced by $P_{O_2}(I) = 10^{-8}$ Pa in the upper chamber and $P_{O_2}(II) = 1$ Pa in the lower chamber. Grain boundary grooves are observed on both the surfaces, of which morphology is similar to that formed by ordinary thermal etching, as reported in previous study.[20] The oxygen potential gradients with combination of the lower P_{O_2} values hardly affect the

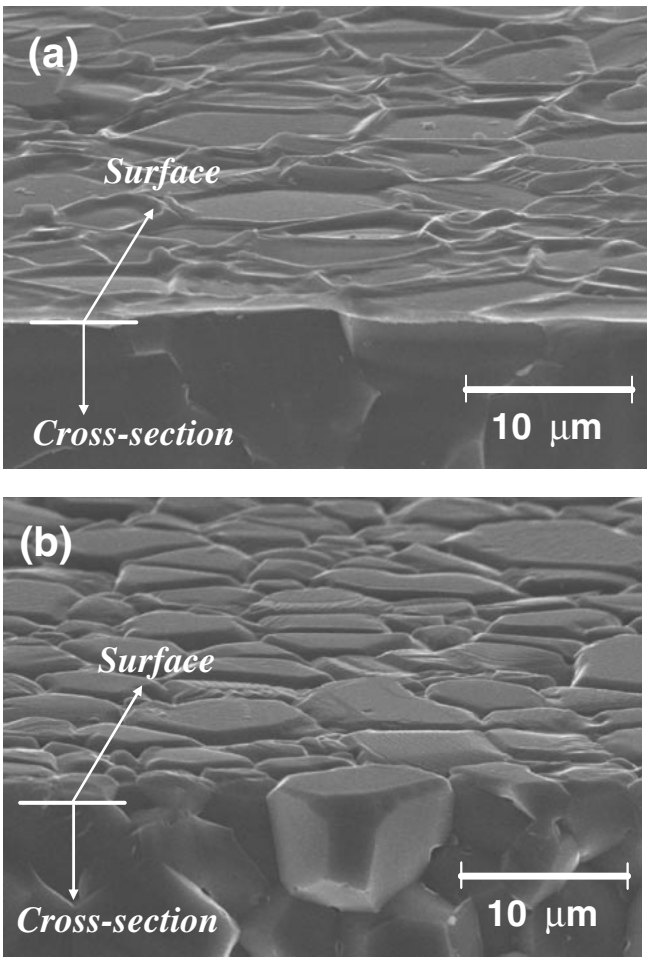

Fig. 6 SEM micrographs of the two surfaces of polycrystalline Al_2O_3 exposed at 1923 K for 10 h under a ΔP_{O_2} with (a) $P_{O_2}(II) = 10^5$ Pa in the upper chamber and (b) $P_{O_2}(I) = 1$ Pa in the lower chamber.

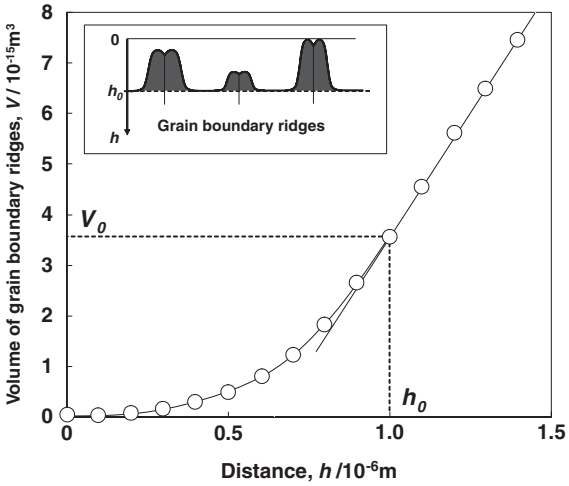

Fig. 7 Volume of grain boundary ridges formed in the measurement area (10^{-8} m^2) on the upper chamber side as a function of distance h for polycrystalline Al_2O_3 exposed at 1923 K for 10 h under a ΔP_{O_2} with $P_{O_2}(II) = 10^5$ Pa in the upper chamber and $P_{O_2}(I) = 1$ Pa in the lower chamber. The zero point of h is set to the top of the highest ridge in the measurement area.

surface morphological change. The absence of the grain boundary ridges suggests that the migration of aluminum was scarcely related to the oxygen permeation. This surface morphology supports the oxygen permeation mechanism with $n = -1/6$ (n-type conduction) as shown in Fig. 4.

Figure 6 shows SEM micrographs of the two-sided surfaces of the Al_2O_3 wafer exposed at 1923 K for 10 h under ΔP_{O_2} between $P_{O_2}(II) = 10^5$ Pa in the upper chamber and $P_{O_2}(I) = 1$ Pa in the lower chamber. They reveal grain boundary ridges having heights of a few micrometers on the surface exposed to the higher P_{O_2}, while deep ditches are formed at the grain boundaries on the surface exposed to the lower P_{O_2}. As mentioned above, if the oxygen permeation mainly progresses by the reaction given by eq. (17), the total volume of the grain boundary ridges is predicted to be comparable with that of Al_2O_3 that corresponds to the amount of oxygen permeation.

Figure 7 shows the volume of the grain boundary ridges formed on the upper chamber side as a function of distance, h, for the Al_2O_3 wafer exposed at the same conditions as that in Fig. 6. The zero point of h is set to the top of the highest ridge in the measurement area. The volume of the grain boundary ridges gradually increases with increasing h, followed by a linear increase above h_0. The volume V_0 at h_0 corresponds to the total volume of the ridges. The calculated oxygen permeability constant, which is estimated by assuming that the amount of permeated oxygen is equal to the oxygen in Al_2O_3 in the volume V_0, is 1.5×10^{-10} mol·m^{-1}s^{-1}. This value is very similar to the experimental one of 1.9×10^{-10} mol·m^{-1}s^{-1} as shown in Fig. 4. This result provides adequate support for the oxygen permeation mechanism with $n = 3/16$ (p-type conduction).

Oxygen permeation under an oxygen potential gradient is found to be controlled by grain boundary diffusion of oxygen and aluminum in regions of lower and higher P_{O_2}, respectively. For the growing Al_2O_3 scale on the alumina forming alloy under a region of lower P_{O_2}, such as that exposed to flow of purified argon,[10] the absence of grain boundary ridges is considered to be mainly due to inward grain boundary diffusion of oxygen through oxygen vacancies. On the other hand, the scale in a region of higher P_{O_2}, such as that exposed to air flow, may exhibit a p-n junction behavior, where outward diffusion of aluminum through aluminum vacancies proceeds in addition to the inward diffusion of oxygen.

3.2 Grain boundary diffusion of oxygen and aluminum

Since the grain boundary width, δ, is not known, values of $D_{gb}\delta$ are estimated from the oxygen permeability constants as shown in Fig. 4 by the procedure described in Section 2.3. Figure 8 shows $D_{gb}\delta$ of oxygen and aluminum as a function of P_{O_2} in the upper chamber at 1923 K. The solid and open symbols indicate the $D_{gb}\delta$ of oxygen and aluminum, respectively. Values of oxygen diffusion from the literature[11,12,14] are also shown in Fig. 8 and they were determined from an ^{18}O isotopic tracer profiling technique for bicrystalline or polycrystalline Al_2O_3 annealed in a homogeneous environment without imposing a oxygen potential gradient, and their P_{O_2} values on the abscissa corresponded to those in the annealing environments. The data of Refs. 12) and 14) are estimated by extrapolating to 1923 K. The $D_{gb}\delta$ of oxygen decreases with increasing P_{O_2}, whereas $D_{gb}\delta$ of aluminum

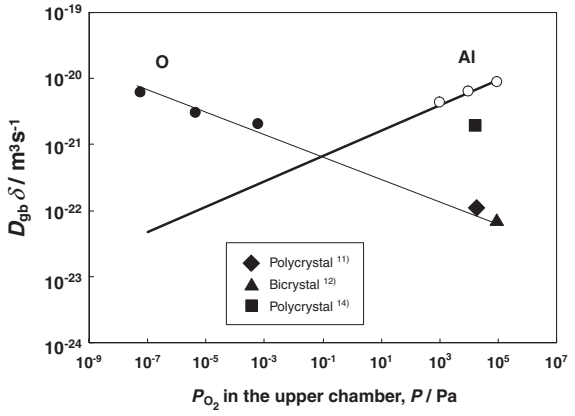

Fig. 8 $D_{gb}\delta$ of oxygen and aluminum in polycrystalline Al_2O_3 as a function of the equilibrium partial pressures of oxygen in the upper chamber at 1923 K. The solid and open symbols indicate the $D_{gb}\delta$ of oxygen and aluminum, respectively. The literature data of oxygen diffusion obtained by isotopic tracer profiling are also shown.[11,12,14]

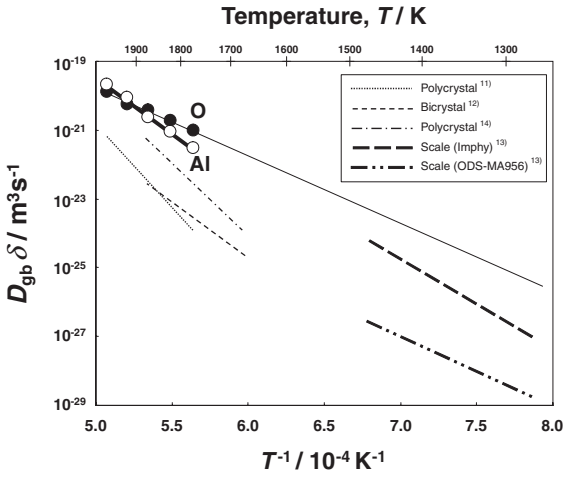

Fig. 9 Arrhenius plots of $D_{gb}\delta$ of oxygen and aluminum in polycrystalline Al_2O_3 together with oxygen diffusion data from the literature.[11–14] The solid and open symbols indicate the $D_{gb}\delta$ of oxygen and aluminum, respectively. These data are calculated from the oxygen permeability constants shown in Fig. 2.

Table 1 Arrhenius parameters, D' and Q, for grain boundary diffusion in α-Al_2O_3 ($D_{gb}\delta = D' \exp(-Q/RT)$).

Diffusional species		Sample	Method	D'/m^3 s^{-1}	Q/kJ mol^{-1}
Oxygen	This work	Polycrystal	Oxygen permeation $P_{O_2}(I) = 10^{-8}$ Pa	4.0×10^{-10}	395
	Prot *et al.*[11]	Polycrystal	Isotopic tracer (SIMS)	1.6×10^{3}	921
	Reddy *et al.*[14]	Polycrystal	Isotopic tracer (NRA)	5.5×10^{1}	825
	Nakagawa *et al.*[12]	Bicrystal	Isotopic tracer (SIMS)	8.4×10^{-6}	627
	Messaoudi *et al.*[13]	Oxide scale	Oxidation of ODS-MA956	2.1×10^{-13}	391
			Oxidation of Imphy	5.3×10^{-7}	505
			Isotopic tracer (SIMS)		
Aluminum	This work	Polycrystal	Oxygen permeation $P_{O_2}(II) = 10^{5}$ Pa	2.8×10^{-4}	611

increases. The line extrapolated to higher P_{O_2} for oxygen diffusion is compatible with previously reported data obtained using SIMS,[11,12] but deviates widely from data obtained using NRA.[14]

There is a thermal equilibrium level of defects such as Schottky pairs[26] or Frenkel pairs[14] in Al_2O_3 exposed under uniform environments at high temperatures. As shown Figs. 4–7, the oxygen potential gradient through the wafer seems to result in the formation of new defects such as oxygen vacancies for lower P_{O_2} ranges (n-type conduction) and aluminum vacancies under higher P_{O_2} ranges (p-type conduction) in addition to the thermally induced defects. Because the $D_{gb}\delta$ of oxygen and aluminum are proportional to the concentration of their respective vacancies, as given by eqs. (14) and (18), the dominant defects in the wafer are probably oxygen vacancies for lower P_{O_2} ranges and aluminum vacancies for higher P_{O_2} ranges. Therefore, the extrapolated line in Fig. 8 may correspond to the SIMS data,[11,12] where the concentration of oxygen vacancies induced by the oxygen potential gradient in the higher P_{O_2} ranges is asymptotic to that under thermal equilibrium. Nevertheless, the reason why the NRA datum deviates so much cannot be ascertained based on the descriptions given in the paper.[14]

Figure 9 shows the Arrhenius plots of $D_{gb}\delta$ of oxygen and aluminum in polycrystalline Al_2O_3 together with oxygen diffusion data from the literature[11–14] obtained by ^{18}O isotopic tracer profiling. The solid and open symbols indicate the $D_{gb}\delta$ of oxygen and aluminum, respectively. These data are determined from the oxygen permeability constants shown in Fig. 3 using eqs. (14) and (18). The $D_{gb}\delta$ values of oxygen and aluminum are calculated at P_{O_2} values of 10^{-7} Pa and 10^5 Pa, respectively. Previously obtained data,[11,12,14] with the exception of that from Ref. 13), were obtained for Al_2O_3 annealed in homogeneous high P_{O_2} environments without any oxygen potential gradients. The data from Ref. 13) were determined for growing Al_2O_3 scales formed on Fe-Cr-Al alloys such as Zr doped (Imphy) and Y_2O_3 doped (ODS-MA956) during the oxidation of the alloys in O_2. Therefore, these scales were subject to steep oxygen potential gradients. Table 1 is also summarizes the Arrhenius parameters (D' and Q) for grain boundary diffusion in α-Al_2O_3 ($D_{gb}\delta = D' \exp(-Q/RT)$). The $D_{gb}\delta$ values of oxygen and aluminum increase with an increase in temperature. The $D_{gb}\delta$ values of oxygen in this study tend to be larger than those given in other reports, including the extrapolated data. The activation energy of the oxygen grain boundary diffusion

in this study is lower than those of the previously obtained data for annealing in homogeneous surroundings, but it is similar to those for Al_2O_3 scales. Oxygen vacancies, which preferentially induced at the grain boundaries by the oxygen potential gradients, is conjectured to decrease a barrier to grain boundary diffusion of oxygen, resulting in the lower activation energy.

The extrapolation of the linear log (oxygen $D_{gb}\delta$) vs. $log(1/T)$ plot in this study to lower temperatures results in a much larger value than those for Al_2O_3 scales. The deviation of the oxygen $D_{gb}\delta$ may be caused by inhibition of the inward grain boundary diffusion of oxygen in the scales due to "site-blocking"[12] of the oxygen reactive elements such as Zr and Y, which are included in the alumina forming alloys and are segregated at the grain boundaries of the scales during oxidation of the alloys.[19] The data in Ref. 13) were determined from ^{18}O depth profiles from the scale surface to a depth of about 250 nm in the Al_2O_3 scales with a thickness of a few micrometers. Because the scales were exposed to steep oxygen potential gradients, the oxygen D_{gb} is considered to increase from the scale surface to the interface between the scale and alloys in proportion to the oxygen vacancy concentration in the scale. The data in Ref. 13) are speculated to correspond to the oxygen $D_{gb}\delta$ at the higher oxygen potential in the subsurface of the scales, whereas the oxygen $D_{gb}\delta$ in this study were estimated at the P_{O_2} of 10^{-7} Pa, which was thought to be considerably lower than the oxygen potential in the subsurface scales. This may be related to the large difference in the values of $D_{gb}\delta$ found in this study and that of Ref. 13), as shown in Fig. 9.

As mentioned above, when the Al_2O_3 wafer was exposed to oxygen potential gradients, oxygen diffused from regions of higher to lower P_{O_2} in *n*-type conduction ranges while aluminum diffused in the opposite direction to the oxygen flux in *p*-type conduction ranges. These phenomena will be useful for elucidating how much each migration of oxygen and aluminum is affected through the grain boundaries of the Al_2O_3 under oxygen potential gradients by the REs segregated at the grain boundaries.

4. Conclusions

The mass-transfer mechanisms in an undoped polycrystalline α-Al_2O_3 wafer were explained by evaluating oxygen permeation through the wafer when it was subjected to oxygen potential gradients at high temperatures. When the wafer was subjected to potential gradients caused by P_{O_2} values below about 1 Pa, O_2 molecules are assumed to permeate mainly by grain boundary diffusion of oxygen through the oxygen vacancies from regions of higher P_{O_2} to regions of lower P_{O_2}. Grain boundary ridges were hardly formed on the surfaces under a higher P_{O_2} because of the very low aluminum flux. Under potential gradients generated by P_{O_2} above about 1 Pa, O_2 molecules seem to permeate mainly by grain boundary diffusion of aluminum through aluminum vacancies from regions of lower P_{O_2} to regions of higher P_{O_2}, resulting in the formation of grain boundary ridge on the higher P_{O_2} surface. The $D_{gb}\delta$ of oxygen estimated from oxygen permeability constants decreased with increasing P_{O_2}, while that of aluminum increased.

Acknowledgment

This work was partially supported by a Grant-in-Aid for Scientific Research on Priority Areas "Nano Materials Science for Atomic Scale Modification 474" from the Ministry of Education, Culture, Sports, Science and Technology (MEXT) of Japan. The authors are grateful to Prof. T. Maruyama, Tokyo Institute of Technology, Assoc. Prof. K. Matsunaga, Kyoto University, Prof. Y. Ikuhara, Dr. N. Shibata, The University of Tokyo, for valuable discussions and advice during the course of this research.

REFERENCES

1) A. G. Evans, D. R. Mumm, J. W. Hutchinson, G. H. Meier and F. S. Pettit: Prog. Mater. Sci. **46** (2001) 505–553.
2) M. Matsumoto, T. Kato, K. Hayakawa, N. Yamaguchi, S. Kitaoka and H. Matsubara: Surf. Coat. Technol. **202** (2008) 2743–2748.
3) N. M. Yanar, G. H. Meier and F. S. Pettit: Scr. Mater. **46** (2002) 325–330.
4) E. A. G. Shillington and D. R. Clarke: Acta Mater. **47** (1999) 1297–1305.
5) M. J. Stiger, N. M. Yanar, M. G. Topping, F. S. Pettit and G. H. Meier: Z. Met. kd. **90** (1999) 1069–1078.
6) S. Takahashi, M. Yoshiba and Y. Harada: Mater. Trans. **44** (2003) 1181–1189.
7) D. Strauss, G. Muller, G. Schmacher, V. Engelko, W. Stamm, D. Clemens and W. J. Quaddakers: Surf. Coat. Technol. **135** (2001) 196–201.
8) M. Ueda, K. Kawamura and T. Maruyama: Mater. Sci. Forum **522–523** (2006) 37–44.
9) H. Schmalzried and W. Laqua: Oxide Metals **15** (1981) 339–353.
10) J. A. Nychka and D. R. Clarke: Oxid. Metals **63** (2005) 325–352.
11) D. Plot, M. Le Gall, B. Lesage, A. M. Huntz and C. Monty: Philos. Mag. A **73** (1996) 935–949.
12) T. Nakagawa, I. Sakaguchi, N. Shibata, K. Matsunaga, T. Mizoguchi, T. Yamamoto, H. Haneda and Y. Ikuhra: Acta Mater. **55** (2007) 6627–6633.
13) K. Messaoudi, A. M. Huntz and B. Lesage: Mater. Sci. Eng. A **247** (1998) 248–262.
14) A. H. Heuer: J. Eur. Ceram. Soc. **28** (2008) 1495–1507.
15) A. E. Paladino and W. D. Kingery: J. Chem. Phys. **37** (1962) 957–962.
16) M. Le Gall, B. Lesage and J. Bernardini: Philos. Mag. A **70** (1994) 761–773.
17) M. B-Ricoult and R. Dieckmann: Ber. Bunsenges. Phys. Chem. **90** (1986) 690–698.
18) F. Millot, J. C. Lorin, B. Klossa, Y. Niu and J. R. Tarento: Ber. Bunsenges. Phys. Chem. **101** (1997) 1351–1354.
19) B. A. Pint, A. J. Garratt-Reed and L. W. Hobbs: J. Am. Ceram. Soc. **81** (1998) 305–314.
20) T. Matsudaira, M. Wada, S. Kitaoka, T. Asai, Y. Miyachi and Y. Kagiya: J. Soc. Mater. Sci., Jpn. **57** (2008) 532–538.
21) H. F. Volk and F. W. Meszaros: *Ceramic Micro Structures their Analysis Significance & Production*, ed. by R. M. Fullhrath and J. A. Pask, (John Wiley and sons, New York, 1968) pp. 636–645.
22) E. L. Courtright and J. T. Prater: *Oxygen Permeability of Several Oxides above 1200°C*, US DOE Rep. PNL-SA-20302 (1992).
23) Y. Ogura, M. Kondo, T. Morimoto, A. Notomi and T. Sekigawa: Mater. Trans. **42** (2001) 1124–1130.
24) J. Pappis and W. D. Kingery: J. Am. Ceram. Soc. **44** (1961) 459–464.
25) K. Kitazawa and R. L. Coble: J. Am. Ceram. Soc. **57** (1974) 245–250.
26) K. Matsunaga, T. Tanaka, T. Yamamoto and Y. Ikuhara: Phys. Rev. B **68** (2003) 085110.

Appendix

In this section, process of deriving eq. (7), which is the

flux of the oxygen permeation, is described. Each charged particle flux is given by inserting eq. (3) into eq. (2).

$$J_i = Z_i j_i = -\frac{\sigma t_i}{Z_i F^2} \cdot \frac{\partial \eta_i}{\partial x} \tag{A·1}$$

The charged particle fluxes are expressed by

$$\eta_{Al} = \mu_{Al} + Z_{Al} F \varphi, \tag{A·2}$$

$$\eta_O = \mu_O + Z_O F \varphi, \tag{A·3}$$

$$\eta_{h^\cdot} = \mu_{h^\cdot} + F \varphi, \tag{A·4}$$

$$\eta_{e'} = \mu_{e'} - F \varphi. \tag{A·5}$$

Inserting Gibbs-Duhem equation (eq. (5)) and eqs. (A·2)–(A·5) into eq. (A·1) and assuming that Fermi energy in the polycrystalline Al_2O_3 wafer is constant give as follows.

$$\begin{aligned} J_{Al} &= -\frac{\sigma t_{Al}}{Z_{Al} F^2}\left(\frac{\partial \eta_{Al}}{\partial x}\right) = -\frac{\sigma t_{Al}}{Z_{Al} F^2}\left(\frac{\partial \mu_{Al}}{\partial x} + Z_{Al} F \frac{\partial \phi}{\partial x}\right) \\ &= -\frac{\sigma t_{Al}}{Z_{Al} F^2}\left(-\frac{|Z_{Al}|}{|Z_O|}\frac{\partial \mu_O}{\partial x} + Z_{Al} F \frac{\partial \phi}{\partial x}\right) \\ &= -\frac{\sigma t_{Al}}{Z_O F^2}\left(\frac{\partial \mu_O}{\partial x} + Z_O F \frac{\partial \phi}{\partial x}\right) \end{aligned} \tag{A·6}$$

$$J_O = -\frac{\sigma t_O}{Z_O F^2}\left(\frac{\partial \eta_O}{\partial x}\right) = -\frac{\sigma t_O}{Z_O F^2}\left(\frac{\partial \mu_O}{\partial x} + Z_O F \frac{\partial \phi}{\partial x}\right) \tag{A·7}$$

$$J_{h^\cdot} = -\frac{\sigma t_{h^\cdot}}{F^2}\left(\frac{\partial \eta_{h^\cdot}}{\partial x}\right) = -\frac{\sigma t_{h^\cdot}}{F} \cdot \frac{\partial \phi}{\partial x} \tag{A·8}$$

$$J_{e'} = \frac{\sigma t_{e'}}{F^2}\left(\frac{\partial \eta_{e'}}{\partial x}\right) = \frac{\sigma t_{e'}}{F} \cdot \frac{\partial \phi}{\partial x} \tag{A·9}$$

The sum of the charged particle fluxes can be expressed using eqs. (4), (6) and (A·6)–(A·9) as follows.

$$\begin{aligned} &J_{Al} + J_O + J_{h^\cdot} + J_{e'} \\ &= -\frac{\sigma(t_{Al} + t_O)}{Z_O F^2}\left(\frac{\partial \mu_O}{\partial x} + Z_O F \frac{\partial \phi}{\partial x}\right) \\ &\quad -\left(\frac{\sigma t_{h^\cdot}}{F} \cdot \frac{\partial \phi}{\partial x} + \frac{\sigma t_{e'}}{F} \cdot \frac{\partial \phi}{\partial x}\right) \\ &= -\frac{\sigma(t_{Al} + t_O)}{Z_O F^2} \cdot \frac{\partial \mu_O}{\partial x} - \frac{\sigma(t_{Al} + t_O + t_{h^\cdot} + t_{e'})}{F} \cdot \frac{\partial \phi}{\partial x} \\ &= -\frac{\sigma(t_{Al} + t_O)}{Z_O F^2} \cdot \frac{\partial \mu_O}{\partial x} - \frac{\sigma}{F} \cdot \frac{\partial \phi}{\partial x} = 0 \end{aligned} \tag{A·10}$$

Equation (A·10) can be rewritten as

$$\frac{\partial \phi}{\partial x} = -\frac{(t_{Al} + t_O)}{Z_O F} \cdot \frac{\partial \mu_O}{\partial x} \tag{A·11}$$

The flux of the oxygen that permeates through the wafer is equal to the sum of J_{Al} and J_O. From eqs. (A·6), (A·7), (A·11), the flux of the oxygen permeation is given by

$$\begin{aligned} J_{TO} = J_{Al} + J_O &= -\frac{\sigma(t_{Al} + t_O)}{Z_O F^2}\left(\frac{\partial \mu_O}{\partial x} + Z_O F \frac{\partial \phi}{\partial x}\right) \\ &= -\frac{\sigma(t_{Al} + t_O)}{Z_O F^2}\left(\frac{\partial \mu_O}{\partial x} - (t_{Al} + t_O)\frac{\partial \mu_O}{\partial x}\right) \\ &= -\frac{\sigma(t_{Al} + t_O)(t_{h^\cdot} + t_{e'})}{Z_O F^2} \cdot \frac{\partial \mu_O}{\partial x}. \end{aligned} \tag{A·12}$$

Inserting eq. (3) into eq. (A·12) gives eq. (7) (eq. (A·13)).

$$\begin{aligned} J_{TO} &= -\left({Z_{Al}}^2 F^2 \frac{C_{Al} D_{Al}}{RT} + {Z_O}^2 F^2 \frac{C_O D_O}{RT}\right)\frac{(t_{h^\cdot} + t_{e'})}{Z_O F^2} \cdot \frac{\partial \mu_O}{\partial x} \\ &= -\left(\frac{{Z_{Al}}^2}{Z_O} C_{Al} D_{Al} + Z_O C_O D_O\right)\frac{(t_{h^\cdot} + t_{e'})}{RT} \cdot \frac{\partial \mu_O}{\partial x} \end{aligned} \tag{A·13}$$